Hybrid Excitation Flux Switching Motor with Permanent Magnet Placed at Middle of Field Coil Slots and High Filling Factor Windings

T. Okada, H. Matsumori, *Member, IEEE*, T. Kosaka, *Member*, *IEEE*, and N. Matsui, *Fellow, IEEE*

Abstract—Design and experimental studies on a hybrid excitation flux switching motor as a traction motor for hybrid electric vehicles drive are presented. A stator body of the motor consists of not only laminated silicon-iron electromagnetic steel and three-phase armature windings, but also both of field excitation coils and permanent magnets working together as a variable field magnetomotive force source. On the other hand, a rotor is composed of just laminated silicon-iron electromagnetic steel with salient poles like switched reluctance motor. To bring out the best in drive performances of the hybrid excitation flux switching motor as a variable flux motor for the application, each material adopted for the stator and rotor body should be designed properly in terms of motor efficiency, maximum torque and power densities and so forth. As some of them, in this paper, thinner silicon-iron electromagnetic steel sheet and permanent magnets with high remanent and low amount of Dysprosium used are applied for achieving higher motor efficiency. Moreover, all coils wound flatwise and edgewise using rectangular wires are introduced to realizing high filling factor for reduced copper losses. Experimental tests using a 60kW prototype of the motor demonstrates the designed motor has good motor efficiency under frequent operating points expected for the target vehicle drive.

Index Terms—Hybrid electric vehicle, hybrid excitation flux switching motor, rectangular wire, traction motor, variable flux motor.

I. INTRODUCTION

AS the issue of global warming become more serious, the CO_2 emissions of automobiles are restricted in year by year in each country. The automobile industries have researched and developed the electrically driven vehicles such as hybrid electric vehicles (HEVs), fuel cell vehicles (FCVs), and electric vehicles (EVs) in order to reduce CO_2 emissions. Currently, most HEVs, FCVs, and EVs implement permanent-

nent magnet synchronous motors (PMSM) as the main traction motor owing to their high efficiency, light weight, and small size [1]-[3]. In the PMSM, in order to achieve high torque at a low-speed region as well as high efficiency by reducing copper loss at low- and middle-speed regions, it would be essentially desirable to design the flux density at the air gap as high as possible. Oppositely, in order to achieve high efficiency at a high-speed region by reducing iron loss as well as the flux weakening current (*d*-axis current) resulting in less copper loss, the flux density at the air gap should be designed as low as possible. These represent a design confliction in the PMSM to achieve high efficiency and high power density over the whole operating speed region in a single traction motor drive system. In order to avoid this problem, many types of hybrid excitation motors (HEMs) have been received much attention in automobile traction drive applications and are being researched and developed [4]-[15]. HEMs can change the flux density at the air gap as a kind of variable flux motors (VFMs) [16]-[20].

The various HEMs have proposed, this paper pays attention to a hybrid excitation flux switching motor (HEFSM) [4], [7]-[11], [14] as one of the feasible items of VFMs. The HEFSM has two the different MMF sources comes from PMs and field excitation coils (FECs), can realize variable field flux by controlling the MMF of FECs. The HEFSM is not only capable of variable field flux, but also has following features; (1) an ease of cooling of all active components such as armature windings, FECs and PMs because they are located at the stator, (2) suitability for high speed rotation because of the simple and rugged rotor structure made only by laminated silicon-iron (SiFe) electromagnetic steel sheets, similar to that of a switched reluctance motor (SRM), and (3) low manufacturing cost because the HEFSM does not require expensive materials such as a soft magnetic composite (SMC) that are needed to form three-dimensional magnetic circuit [5] [13] [15]. As a VFM, the HEFSM is expected to be able to achieve better motor efficiency at the high-speed and low-torque region compared with that of the PMSM while achieving the same torque density and the maximum torque as it is because of these features.

The authors have already designed HEFSM and validate the usefulness of HEFSM for HEV drive applications in [7], [8] and [11]. As target specifications in the design of HEFSM, the maximum speed, maximum power, and maximum torque were set to 13,500 r/min, 60 kW, and 207 N·m, respectively. These target values were extracted from the interior permanent magnet

T. Okada and H. Matsumori are with the Department of Electrical and Mechanical Engineering, Graduate School of Engineering, Nagoya Institute of Technology, Gokiso, Showa, Nagoya, 466-8555 Japan.

T. Kosaka is with the Frontier Research Institute for Information Science, Nagoya Institute of Technology, Gokiso, Showa, Nagoya, 466-8555 Japan (kosaka@nitech.ac.jp).

N. Matsui is the emeritus professor, Nagoya Institute of Technology, Gokiso, Showa, Nagoya, 466-8555 Japan.

OKADA et al. : HYBRID EXCITATION FLUX SWITCHING MOTOR WITH PERMANENT MAGNET PLACED AT MIDDLE OF FIELD COIL SLOTS AND HIGH FILLING FACTOR WINDINGS

249

synchronous motor (IPMSM) implemented on the TOYOTA third-generation PRIUS model year 2010 [2]. As the result of studying the power and torque characteristics depending on the magnet position, it is clarified in [9] and [11] that the HEFSM with PMs placed at middle of FECs slots has a good balance of high power and high torque, and can achieve high motor efficiency. However, the motor efficiency of the HEFSM in [11] is slightly lower than that of the IPMSM implemented on the TOYOTA third-generation PRIUS model year 2010 [2]. In the low-speed operating region, the copper loss is the main loss and decreases the motor efficiency. On the other hand, in the high-speed operating region, the largest loss is an iron loss, resulting in the degradation of motor efficiency. Also, the PMs used in the HEFSM in [11] contain a large amount of rare-earth in order to avoid their demagnetization. However, HEV drive applications have to reduce the material cost for production in large quantities, and the dysprosium (Dy) is known as the most expensive heavy rare-earth material in neodymium -iron- boron (NdFeB) magnets.

In this paper, the authors report the results of the design study of HEFSM aiming at the improvement of the efficiency in all operating regions and cost reduction by applying new materials such as high filling factor windings using flat-wise wire, edge-wise wire, thin electromagnetic steel, and PMs with high remanent magnetization under the reduced amount of Dy. The design flow of the HEFSM using the new materials shown above is introduced in Section IV. Based on the design results, an experimental motor is built and experimental performance evaluation test results are demonstrated in Section V. Finally, in order to improve the design accuracy at FEA design stage, root causes of the error between the calculated and the measured values of iron loss and the reduction studies on the error are discussed in Section VI.

II. CONFIGURATIONS OF HEFSM AND BASIC WORKING PRINCIPLE AS VFM

A. Machine Structure

Fig. 1 shows a two-dimensional cross-sectional view of HEFSM which is a research objective in this paper. As shown in Fig. 1, the HEFSM consists of the stator with 24 coil slots and the rotor with 10 salient poles. In our prior studies [21]-[24], various slot-pole combinations have been examin
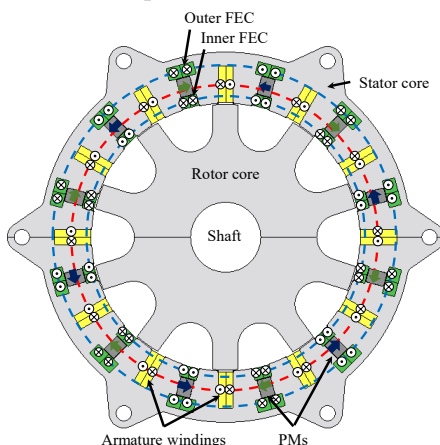
ined. As a result, this combination is selected in this study from the viewpoint of lower cogging and pulsating torque and higher maximum torque capability. All active components such as three-phase armature windings, PMs, and FECs are located at the stator, as mentioned earlier. Similar to that of SRM, the rotor consists of only laminated SiFe electromagnetic steel. It is appropriate for high-speed drive applications. Since the rotor has 10 salient poles, this HEFSM works as 10 pole pairs machine because of the magnetic circuit configuration.

B. Basic Working Principle

Fig. 2 depicts the magnetic flux paths at no FECs excitation and at FECs excitation. As shown in Fig. 2(a), the amount of the PM flux passing through the air gap is small at no FECs excitation condition. This is because the PM flux path is the short-circuit path flowing from the N pole to the S pole of the PM. The flux through the back-yoke iron outside of the outer FEC slots. For the above reason, the iron loss and the back-EMF can be reduced in the high-speed region. Oppositely, at FECs excitation condition, the magnetic flux produced by the MMF of FECs does not pass through PMs, but passes through the air gap as shown by the red line in Fig. 2(b). Moreover, the PM flux path changes from the short-circuit path to one through the air gap. The amount of the flux linkage of armature windings is the sum of the magnetic fluxes generated by the PMs and the MMF of FECs. The field strengthening control produces high torque and reduces copper loss by increasing back-EMF coefficient.
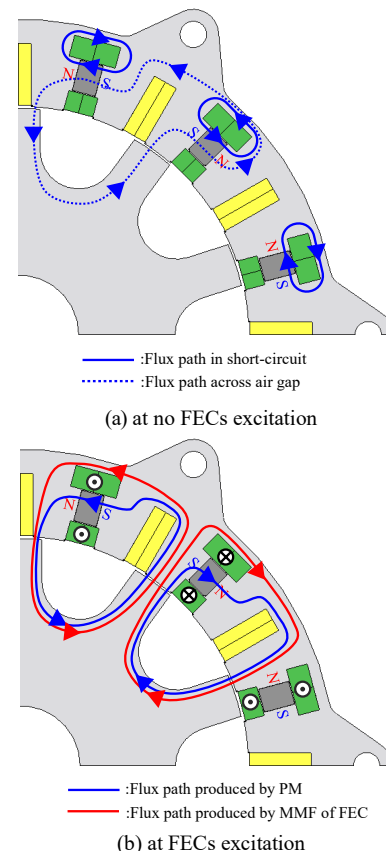

—— :Flux path in short-circuit
······ :Flux path across air gap

(a) at no FECs excitation

—— :Flux path produced by PM
—— :Flux path produced by MMF of FEC

(b) at FECs excitation

Fig. 2. Flux paths produced by PMs and MMF of FECs with and without field coil excitation.

Fig. 1. Sectional view of HEFSM.

III. TARGET SPECIFICATIONS OF THE HEFSM AND PROBLEMS OF THE CONVENTIONAL TEST MOTOR

A. Design Constraints and Target Specifications

The design constraints and target specifications of the proposed machine for automobile traction drive applications are listed in Table I. Most of the values are based on the specifications of the IPMSM adopted in the TOYOTA third-generation PRIUS model year 2010 hybrid synergy drive system [2]. The total axial length of the motor, including the height of the coil-end, is limited to less than 120 mm and the outer diameter of the stator is fixed at 264 mm. The total weight of PMs used is limited to be less than 0.75 kg, and the air gap length is fixed at 0.8 mm. The electrical constraints associated with inverter specifications such as the maximum current, the maximum DC-bus voltage, and the withstand voltage of switching device are set to be the same as those in the IPMSM drive system [2] in Table I. As thermal constraints, assuming that the same cooling system as the IPMSM drive system [2] is adopted, the maximum current densities for three-phase armature windings and FECs are set to 26 Arms/mm2. As target specifications, the maximum speed, maximum power, and maximum torque are set to 13,500 r/min, 60 kW, and 207 N·m, respectively. The authors already have conducted the experimental evaluation tests for several HEFSMs [7] [8] [11]. Based on the results, it has been known that the measured value has been lower than the values computed by three-dimensional finite element analysis (3D-FEA). Taking this fact into consideration, the target values at 3D-FEA design stage are set to be higher than those achieved by the IPMSM as shown in Table I in order to make it possible achieve the target maximum power and torque in real fabricated HEFSM.

TABLE I
DESIGN CONSTRAINTS AND TARGET SPECIFICATIONS

Items	IPMSM PRIUS2010	HEFSM
Stator outer diameter [mm]	264	264
Motor axial length [mm]	120	<120
Air gap length [mm]	0.8	0.8
Permanent magnet weight [kg]	0.768	<0.75
Max. DC-bus voltage inverter [V]	650	650
Withstand voltage of switching device [V_{0-p}]	1,200	1,200
Max. inverter current [Arms]	170	170
Max. current density in armature winding [Arms/mm^2]	26	26
Max. current density in FEC [A/mm^2]	NA	26
Maximum torque [Nm] (real target)	207	>207
Maximum torque [Nm] (3D-FEA)	NA	>220
Maximum power [kW] (real target)	60	>60
Maximum power [kW] (3D-FEA)	NA	>68.2
Maximum speed [r/min]	13,500	13,500

B. Problems of Previously Tested HEFSM

The maximum power and torque measured in previously fabricated HEFSMs under the limitations related to the inverter were 60.2 kW and 207.7 N·m that satisfied the target maximum power and torque of 60 kW and 207 N·m shown in Table I,

respectively. However, there were two problems remaining as follows.

At first, the PMs employed contain a large amount of Dy in their composition to avoid their demagnetization at the maximum temperature of 180 °C expected for automotive applications. To reduce the amount of Dy used while keeping the maximum power and torque densities as high as possible, the HEFSM with PMs placed at the middle of FECs slots has been selected [11]. The directions of magnetic fields produced by MMF of FECs in two HEFSMs with PMs placed at middle and at bottom of FECs slots are shown in Fig. 3. As shown in the figure, in the case of the HEFSM with PMs placed at the middle of FECs slots, the direction of the magnetic field produced by the MMF of outer FECs becomes a reverse magnetic field to the PMs. Although the MMF of outer FECs can elevate the maximum torque density [11], this promotes irreversible demagnetization of the PMs under the field strengthening control at high temperature. In contrary, in the case of the HEFSM with PMs placed at the bottom of FECs slots, the direction of the magnetic field generated by the MMF of inner FECs is a forward magnetic field to the PMs and therefore, irreversible demagnetization can be perfectly avoided under the field strengthening control at high temperature. As the HEFSM with PMs placed at the middle of FECs slots also has inner FECs, the irreversible demagnetization is mitigated compared with the HEFSM with only outer FECs [11]. Even so, the HEFSM shown in Fig. 3(a) needs the PMs with higher coercivity. In other words, it requires the PMs with a larger amount of Dy used compared with the HEFSM shown in Fig. 3(b). To reduce the amount of Dy used is a problem to be solved from the viewpoints of low cost and saving rare-earth material.

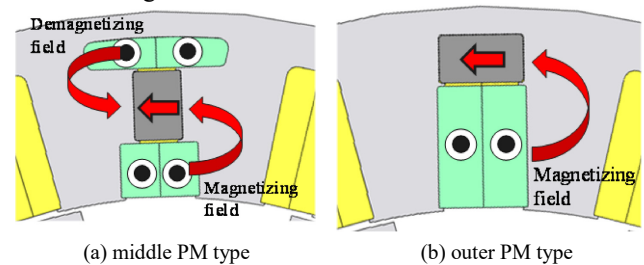(a) middle PM type   (b) outer PM type
Fig. 3. Flux paths of two types of HEFSMs.

Secondly, the problem is that the motor efficiency is worse than the IPMSM as an objective of the comparison. Table II appears the motor efficiency under the frequent operating points as a traction motor for a target vehicle drive. In Table II, η_m means motor efficiency. P_{ca} and P_{cf} are the copper losses dissipated in armature windings and FECs at their temperature of 100 °C, respectively. Pi is an iron loss, which is calculated by subtracting the motor output power, the mechanical loss, and the sum of the copper losses from the motor input power. It is confirmed that the motor efficiency is significantly lower than that of the IPMSM. The main loss is the copper loss, which deteriorates the motor efficiency at the heavy-load condition such as the operating points of No. 2 and 4. At the high-speed operating points of No. 6, 7 and 8, the motor efficiency falls down due to a large iron loss as the main loss. In addition, the

copper loss in FECs occurs in spite of the light-load and low-speed conditions such as the operating points of No. 1, 3 and 5. This is because the PM flux linkage of armature coil is insufficiently small and thus, the field strengthening control by FECs has to be applied even in the light-load condition. For the above reason, the motor efficiency of the previously tested motor is lower than that of the IPMSM, which is another issue to be overcome for low energy consumption electrically driven vehicles.

The problems to be solved in the previously tested HEFSM can be summarized specifically as follows.

- ・High copper loss in the heavy-load region
- ・High iron loss in the high-speed region
- ・PMs containing a large amount of Dy
- ・Insufficiently small PM flux linkage of armature winding

TABLE II
MEASURED EFFICIENCY AND LOSS BREAKDOWN OF PREVIOUSLY FABRICATED HEFSM

Operating points			IPMSM	Previously fabricated HEFSM Measured			
No.	N [r/min]	T [Nm]	η_m [%]	η_m [%]	P_{ca} [W]	P_{cf} [W]	P_i [W]
1	1,000	13	88.5	84.7	143	43	60
2	1,000	75	89	79.6	850	829	349
3	2,000	13	89.5	89.4	135	49	134
4	2,000	130	90.5	82.9	1,981	2,317	1,339
5	3,000	13	90	88.2	141	58	333
6	6,000	13	91	90	120	127	592
7	8,000	13	91	89	110	152	986
8	10,000	13	92	87.7	111	219	1,268

IV. DESIGN OF HEFSM TO OVERCOME THE PROBLEMS

This section introduces the design flow of HEFSM which realizes high efficiency and low cost. To remedy the above four problems, material changes and design policies in this design are listed specifically as follows [25].

1) Change from round wire to flat-shape rectangular wire,
2) Replace with thinner electromagnetic steel,
3) Change to the PM with high remanent magnetization and low amount of Dy used and,
4) Increase in the PM flux linkage at no field coil excitation. The HEFSM with the PMs placed at the middle of FECs slots is designed by using a commercially available FEA package, JMAG-Designer Ver.16.0 (JMAG) [26]. Fig. 4 illustrates the design flow of the HEFSM. The HEFSM designed employs a SiFe electromagnetic steel 30JNE1500 with 0.3 mm thickness for low iron loss replaced with 35HX250 with 0.35mm thickness used in the previously tested HEFSM. The previously tested HEFSM employed the PMs with the type N46UH-G, which Shin-Etsu Chemical Co. Ltd., made in new alloying process by grain boundary diffusion. In this design study, we select a PM of type N48TS-GR, which has higher remanent flux density and lower coercivity than those of N46UH-G. To increase the PM flux linkage at no FECs excitation, it is also necessary to make the PM surface perpendicular to its

magnetization direction as large as possible. According to Table I, however, the amount of PMs used is limited, and therefore, the PM thickness along with the magnetization direction becomes thinner so that irreversible demagnetization of the PM is likely to occur. In addition, it prevents from increasing the MMF of outer FECs that contributes to an increase in the maximum torque. Therefore, as shown in process 2 in Fig. 4, the optimum PM shape is searched in order from the PM shape with the largest PM surface. For this reason, by repeating the processes 1 to 5 as shown in Fig. 4, the optimum PM type and its dimensions, and coil slot shapes are determined for getting the maximum PM flux linkage at no FECs excitation while satisfying the target specifications listed in Table I. The irreversible demagnetization of the PM has been evaluated by 3D-FEM at
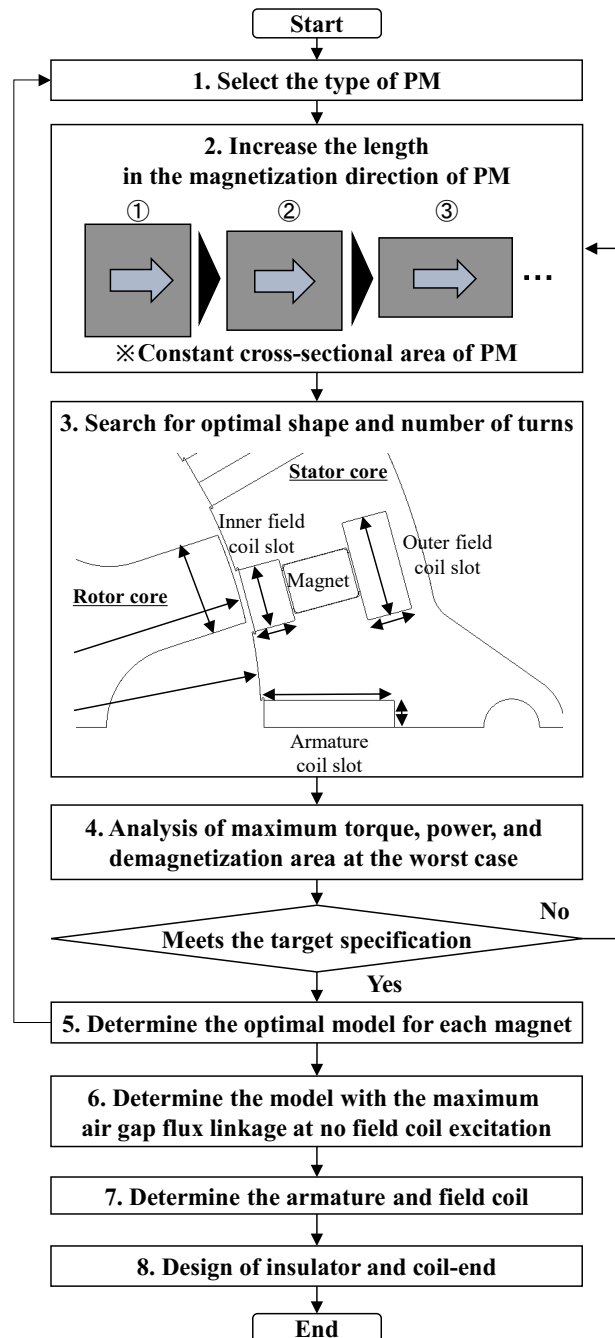

Fig. 4. Flowchart of design for the HEFSM.

the magnet temperature of 180 °C which is the maximum temperature assumed for the target automotive application. The ratio of demagnetization volume to the total magnet volume is set to 5% or less as the target demagnetization ratio. The details of the irreversible demagnetization evaluation are given in [25]. Finally, after the optimum PM type and dimension are decided, determination of high filling factor coil specifications using rectangular wires, detailed design of the insulator and coil-end, and fine adjustment of various dimensions are conducted as shown in the processes 7 and 8. Please refer to Ref. [25] about further design details of the armature and field excitation coils with high filling factor using rectangular-shape wire.

V. PERFORMANCE EVALUATION

A. Test Motor Specifications

Figs. 5 and 6 are an external view of the newly designed HEFSM and enlarged sectional views of the stator body for the previously designed and the newly designed motors, respectively. Fig. 7 shows photographs of the newly designed test motor built for the purpose of dive performance evaluation. Tables III and IV appear the material used, the machine parameters and the dimensions of the newly designed test motor including those of the previously designed HEFSM. Due to manufacturing problems of the rectangular-shape conductors, the total axial length is 129 mm which exceed 120 mm given as the design constraints in Table I. With the exception of this point, the new HEFSM is well designed in accordance with the design procedures. The outer FECs are directly wound into corresponding slots flatwise. Both the inner FECs and the armature coils consist of cassette coils wound edgewise and are inserted from each slot opening into each slot. Welding is performed at the connection side to connect each coil in series. Table V summarizes comparisons of the coil filling factors and the resistances of all coils measured in the previous and the newly designed test motors. By changing from round wires to flat-shape rectangular wires [27], the coil filling factor of each coil is greatly improved so that the resistances of armature winding per phase and outer FECs are considerably reduced. Although the resistance of inner FECs increases due to the difference in the number of turns, the copper loss of inner FECs can be reduced owing to less current. In other circumstances, rotor stress analysis at the maximum speed of 13,500 r/min has been also conducted. As a result, the maximum stress of 92.8 MPa has been found at the portion near the shaft. As this value is enough smaller than the yield point 400 Mpa of the electromagnetic steel sheets used, it is reasonable to suppose
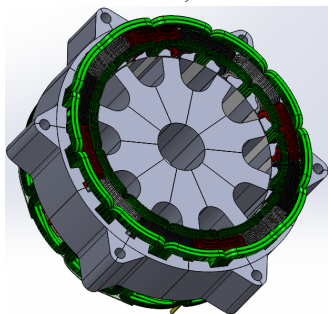
that the newly designed HEFSM has enough mechanical durability even in continuous maximum speed operation. In addition, as a result of the irreversible demagnetization evaluation, the volume demagnetization factor has been 1.34%. Therefore, the newly designed HEFSM can maintain torque performance even during continuous operation at the maximum temperature.
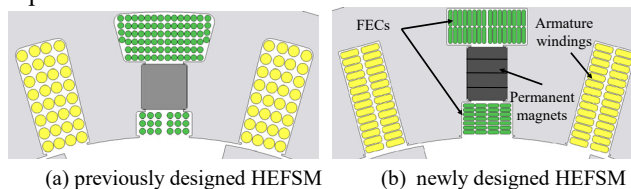

(a) previously designed HEFSM   (b) newly designed HEFSM

Fig. 6. Comparison of the main part of two HEFSMs.

(a) stator core (under assembling)   (b) stator assembly

(c) rotor assembly   (d) overview
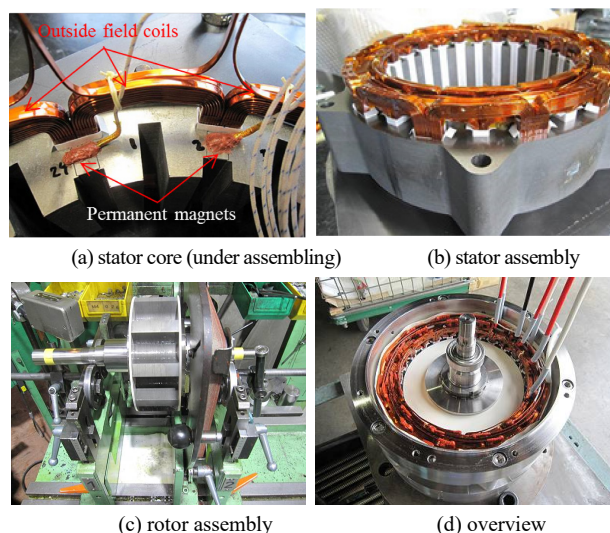
Fig. 7. Photographs of the newly designed test motor.

TABLE III
NEWLY DESIGNED TEST MOTOR SPECIFICATIONS

Major dimensions and specifications	Stator outer diameter [mm]	264
	Motor total axial length [mm]	129
	Motor core stack length [mm]	64
	Coil-end length(connection) [mm]	39
	Coil-end length(non-connection) [mm]	26
	Rotor outer diameter [mm]	189.4
	Air gap length [mm]	0.8
	Shaft diameter [mm]	50
	Type of electromagnetic steel	30JNE1500
Armature winding's specifications	No. of turns/coil	14
	Type of connection	3Φ-Y
	Filling factor	0.7
Field winding's specifications	No. of turns/outside coil	16
	Filling factor of outside coil	0.69
	No. of turns/inside coil	14
	Filling factor of inside coil	0.63
Permanent magnet specifications	Type of permanent magnet	N48TS-GR
	Permanent magnet weight [kg]	0.746
Machine parameters	Armature wdg. resist./phase [Ω]	0.037(20°C)
	Outside field wdg. resist. [Ω]	0.258(20°C)
	Inside field wdg. resist. [Ω]	0.352(20°C)

Fig. 5. External view of the newly designed HEFSM.

OKADA et al. : HYBRID EXCITATION FLUX SWITCHING MOTOR WITH PERMANENT MAGNET PLACED AT
MIDDLE OF FIELD COIL SLOTS AND HIGH FILLING FACTOR WINDINGS

253

TABLE IV
USED MATERIALS AND SPECIFICATIONS OF NEWLY DESIGNED TEST MOTOR

Item	Previous test motor	Newly de-signed test motor
Motor core stack length [mm]	62	64
Type of electromagnetic steel	35HX250	30JNE1500
Type of permanent magnet	N46UH-G	N48TS-GR
No. of turns/coil	16	14
No. of turns/outside coil	40	16
No. of turns/inside coil	9	14
Permanent magnet weight [kg]	0.7464	0.7464

TABLE V
COIL FILLING FACTOR AND RESISTANCE OF EACH COIL OF AT 100 °C OF
DESIGNED HEFSM

	Coil filling factor [%]		Resistance [Ω] (@100°C)	
	Previous test motor	Newly designed test motor	Previous test motor	Newly designed test motor
Armature winding	50.6	70.1	0.078	0.049
Inner FECs	40	62.7	0.39	0.46
Outer FECs	53.1	69.4	1.78	0.34

B. Experimental Setup

Fig. 8 shows an experimental setup of the test motor. The experimental performance evaluation test of the test motor is performed using the large capacity and high speed dynamo set up manufactured by SINFONIA TECHNOLOGY CO., LTD. The test motor is coupled with the dynamo set up. The dynamo set up keeps motor speed constant and can evaluate the power up to 175 kW and the torque up to 400 N·m at the test speed in the range of 0 to 20,000 r/min. The average torque meter (MGCplus: HBM Corp.) is used for calculating the torque by integration gross. The rotor position information with 20,480ppr is generated using the resolver manufactured by TAMAGAWA SEIKI CO., LTD through R/D converter. DSP based system (PE-EXPERT III: Myway-Plus Corp.) is used as a controller. The three-phase inverter (MWMES-111087: Myway-Plus Corp.) is used for armature windings excitation. It can supply current of up to 450Arms and its DC-bus voltage is controlled from 200 V to 650 V depending on operating points. The DC chopper (MWINV-5022A: Myway-Plus Corp.) is used for FECs excitation and can supply current of up to 146 DCA and its DC-bus voltage is fixed at 200 V. The digital power meter (WT3000: Yokogawa Electric Corp.) is used for measuring the current, voltage, and input power of armature windings and FECs. Up to the base speed (2,300 r/min in this study), continuous pulse width modulation (CPWM) control with the switching frequency of 12.5 kHz is implemented for the three-phase armature windings current control. Beyond the base speed, 6-step voltage control is performed. Related to operating conditions, the lead angle of the applied voltage is adjusted.
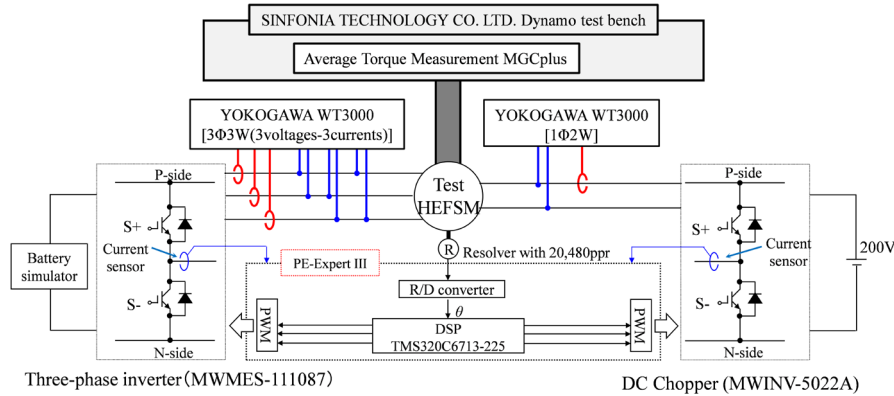

Fig. 8. Experimental setup.

C. Torque-Armature Current-FEC Current Curves

Fig. 9 shows the measured and calculated torque - armature current - FEC current curves for various excitation conditions of armature and field currents. The armature current is supplied from 0 to 170 Arms under the fixed condition of the current lead angle $\beta = 10$ deg. The current density of armature windings at 100 % excitation is 26 Arms/mm^2. The inner and outer FECs currents are adjusted from 0 to 62 DCA and from 0 to 100 DCA, respectively. At maximum excitation condition, the total MMF of both the inner and outer FECs is 2468 AT (i.e. 2468 AT = 14 T × 62 DCA + 16 T × 100 DCA). At maximum excitation condition, both the current densities of the inner and outer FECs become also 26 A/mm2. In the measurement, the rotor rotational speed is fixed at 500 r/min. The measured currents-torque curves and those calculated by 3D-FEA agree well. The maximum torque measured under the maximum armature current and field currents is 212.5 N·m, which satisfies the target maximum torque of 207 N·m shown in Table I.

D. Maximum Torque and Power vs. Speed Curves

Fig. 10 shows the maximum torque and power curves with respect to the motor speed measured under the current and voltage limitations. The maximum power measured under the maximum DC-bus voltage of the three-phase inverter is 67.6 kW at 6,000 r/min, which satisfies the target maximum power of 60 kW shown in Table I. From Fig. 10, it can be confirmed that the difference between the measured power and the calculated power by the 3D-FEA is large in the high-speed

region. The reason for this phenomenon is considered to be that the iron loss is not taken into account in 3D-FEA. At the maximum power at 13,500 r/min, as the iron loss of as much as 13.6 kW occurs, an effect of the iron loss on output power cannot be ignored under 6-step voltage control. The analysis method of the output power taking account of the iron loss is future work.
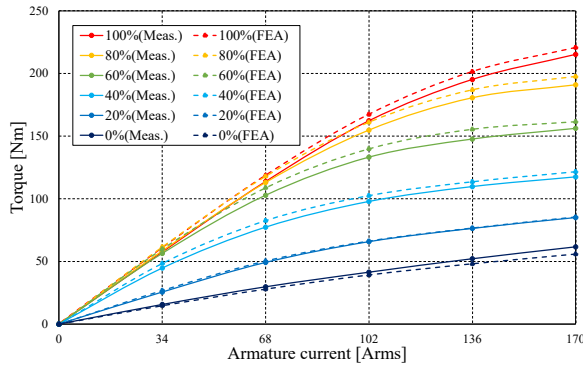

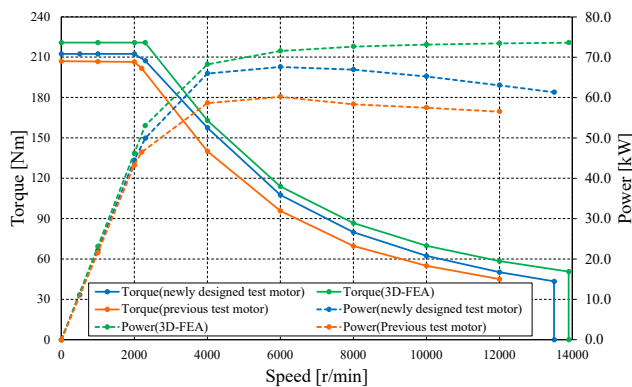Fig. 9. Measured torque-armature current-FEC current curves.

Fig. 10. Measured torque and power vs. speed characteristics.

E. Motor Efficiency

Figs. 11 and 12 depict the motor efficiency maps measured in the previously designed and the newly designed HEFSMs, respectively. Compared to the motor efficiency of the previously designed HEFSM, it is confirmed that the motor efficiency of the newly designed HEFSM is well improved at all operating regions thanks to copper loss reduction by employing the high filling factor windings as well as iron loss reduction by adopting the thinner SiFe electromagnetic steel with lower iron loss. Table VI appears the motor efficiency and the motor loss analysis results at the frequent operating points based on the experimental results of two test motors including the computed values in the newly designed motor. For the purpose of comparison, Table VI also includes the measured motor efficiency of the IPMSM[2]. In Table VI, the motor efficiency is measured under the current condition where the motor efficiency is maximized by considering the sum of copper and the iron losses based on measurement data of currents-torque characteristics while realizing the reference torque. In addition, the iron loss is computed by 3D-FEA in accordance with the current conditions in measurements. From Table VI, the measured motor efficiencies of the newly designed HEFSM at the light-load operating points No. 1, 3,

and 5 to 7 are 0.3-2.0% higher than those of the IPMSM. On the other hand, the measured motor efficiencies at the heavy-load operating points No. 2 and 4 are significantly lower than those of the IPMSM and hence, it is indispensable to improve the motor efficiency at the heavy-load operating points in order to drive the newly designed HEFSM using the same cooling system installed in the IPMSM [2] in the future work. In other circumstances, the measured motor efficiency of the newly designed HEFSM falls down on the whole compared with the motor efficiencies calculated by 3D-FEA. This is mainly because the measured iron loss values at each operating point are considerably higher than the calculated values. To design high efficiency motor accurately, this underestimation of iron loss in 3D-FEA must be conquered.
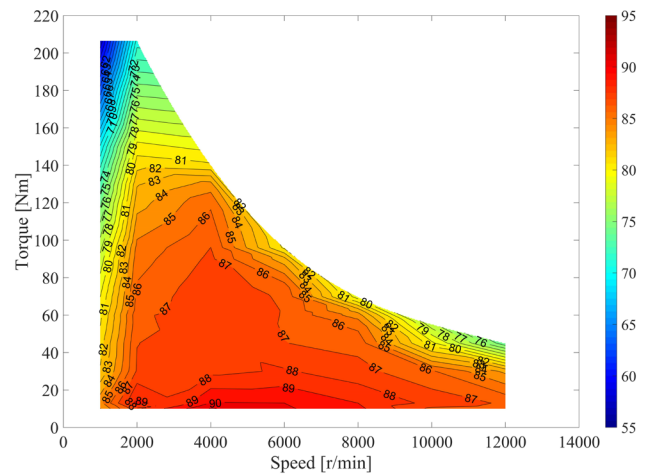

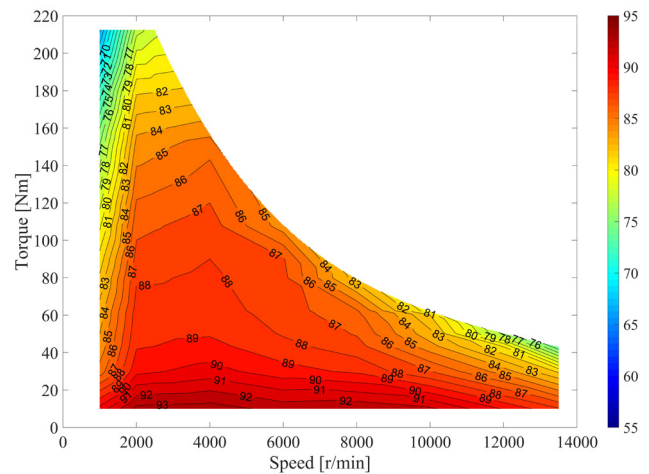Fig. 11. Measured motor efficiency map of the previously designed HEFSM

Fig. 12. Measured motor efficiency map of the newly designed HEFSM.

VI. IRON LOSS COMPUTATION IN 3D-FEA

As can be seen from Table VI, the measured motor efficiency was lower than the those of calculated values because of the large error between the calculated and the measured iron losses. In particular, at the heavy-load operating points No. 2 and 4, the errors are considerably large and therefore, root causes of the error are examined for improving the accuracy of iron loss computation at the motor design stage.

TABLE VI
MEASURED MOTOR EFFICIENCY AND LOSS ANALYSIS RESULTS

Operating points			IPMSM	Previously designed HEFSM				Newly designed HEFSM						
				Measured				Measured				Calc. (3D-FEA)		Error
No.	N [r/min]	T [N·m]	η_m [%]	η_m [%]	P_{ca} [W]	P_{cf} [W]	P_i [W]	η_m [%]	P_{ca} [W]	P_{cf} [W]	P_{imeas} [W]	η_m [%]	P_{icalc} [W]	P_{icalc}-P_{imeas} [W]
1	1,000	13	88.5	84.7	143	43	60	89	105	0	46	91	12.3	-33.7
2	1,000	75	89	79.6	850	829	349	83.1	610	692	309	85.3	67.3	-242
3	2,000	13	89.5	89.4	135	49	134	91.5	96	35	79	93.4	21.1	-57.9
4	2,000	130	90.5	82.9	1,981	2,317	1,339	86.2	1,209	1,905	1,137	88.8	228	-909
5	3,000	13	90	88.2	141	58	333	91.7	96	35	167	94.6	38	-129
6	6,000	13	91	90	120	127	592	92	83	55	423	95.5	105	-318
7	8,000	13	91	89	110	152	986	91.3	75	79	607	95	155	-452
8	10,000	13	92	87.7	111	219	1,268	90.4	81	108	790	93.9	237	-553

A. Root Cause of Error in Iron Loss Calculation

There seem to be two root causes for the error between the calculated and the measured iron losses shown in Table VI.

As the first root cause, the eddy current loss is generally calculated by inputting pure sinusoidal current for the armature windings and pure DC currents for FECs. Assuming an ideal sinusoidal motor model, the flux linkages in the d- and q-axis of HEFSM under conventional current vector control is given in,

$$\begin{bmatrix} \psi_d \\ \psi_q \end{bmatrix} = \begin{bmatrix} L_d & 0 \\ 0 & L_q \end{bmatrix} \begin{bmatrix} I_d \\ I_q \end{bmatrix} + \begin{bmatrix} M_{df}I_f + \psi_{PM} \\ 0 \end{bmatrix} \quad (1)$$

where, L_d, L_q, I_d and I_q follow custom, namely, d- and q-axis inductance and d- and q-axis current, respectively. M_{df} and I_f are the mutual inductance between the FECs and the d-axis winding, and the FEC current, respectively. ψ_{PM} is the PM flux linkage of the armature windings. In the experimental measurements, the armature current actually includes low order current harmonics due to space harmonics included in machine parameters such as L_d, L_q, M_{df} and ψ_{PM}, and high order current harmonics caused by the PWM carrier components under PWM voltage control. The FECs current also contains low order and high order currents harmonics. In order to reduce the computation time of trial and error at the design stage using 3D-FEA, in general, pure sinusoidal armature current is inputted to armature windings and pure DC currents are inputted to FECs. So, it should be considered that the flux distribution in the motor reproduced by 3D-FEA, which is given in (1), is different from that in the experimental test. Taking account of the harmonics contained in the d- and q-axis flux linkage, the eddy current loss is given in the following fashion.

$$P_e = \sum_{n=1} C_{en}(nf)^2 B_{mn}^2 = C_{e1}f^2 B_{m1}^2 + C_{e2}(2f)^2 B_{m2}^2 + \cdots \quad \ldots\ldots\ldots (2)$$

C_{en} is an eddy current loss coefficient of the nth order component, B_{mn} is an amplitude of flux density of the nth order component. According to (2), the eddy current loss produced by the harmonic components in the second and subsequent terms in (2) is not correctly considered in the usual 3D-FEA computation. Missing this computation would be considered as the main reason why the underestimation in Table VI is happening.

The second root cause is the fact that the eddy current loss consumed in the iron core is only considered. In other words, an eddy current losses occurring at flat-shape rectangular wires, PMs, frame and bracket are not taking into account. In real, however, since fluxes leak to the motor components other than the iron core due to an effect of magnetic saturation of the iron core, the eddy current losses occur in these non-iron components. Figs. 13, 14, and 15 demonstrate the analysis results of magnetic flux density distribution in the motor core, the frame and the bracket, and the windings at operating point No. 2 and 4, respectively. From these figures, it can be found that the magnetic flux leaks to other motor components due to the effect of magnetic saturation in the motor core.

In the next subsection, an analysis method taking the above two points into account is examined to reduce the error between the calculated and the measured iron losses.
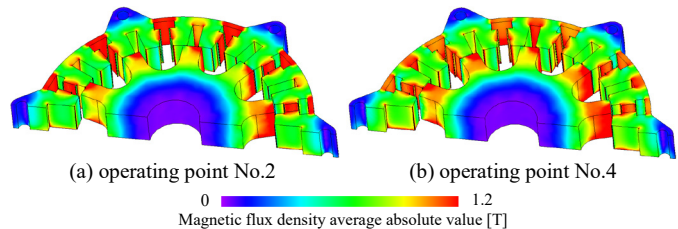

(a) operating point No.2   (b) operating point No.4

0 ▬▬▬ 1.2
Magnetic flux density average absolute value [T]

Fig. 13. Flux density distribution in the motor core at operating point No.2 and 4.

(a) operating point No.2   (b) operating point No.4

0 ▬▬▬ 0.02
Magnetic flux density average absolute value [T]
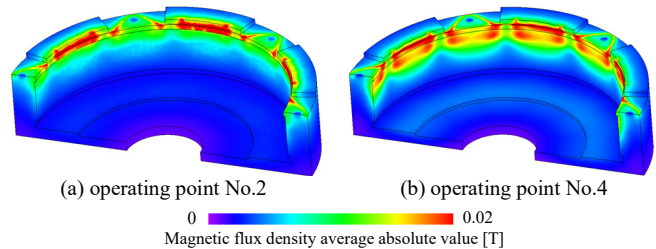
Fig. 14. Flux density distribution in the flame and bracket at operating point No.2 and 4.

(a) operating point No.2   (b) operating point No.4

0 ▬▬▬ 0.5
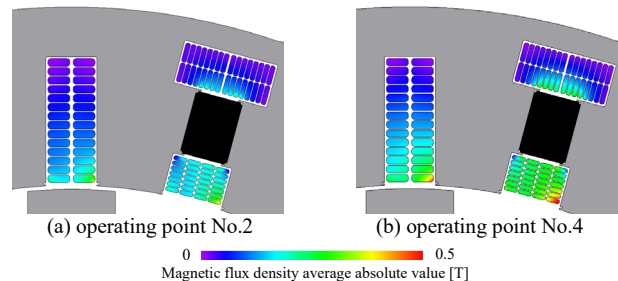Magnetic flux density average absolute value [T]

Fig. 15. Flux density distribution in the winding at operating point No.2 and 4.

B. Analysis Method for Reducing the Error

With setting up conductivity and permeability of each material used, eddy current distribution can be calculated directly from the time and space distribution of flux density of each motor component. Although it is time consuming, this offers the possibility of more accurate calculation of eddy current loss in each component on 3D-FEA. In addition, this analysis enables to more accurately calculate the eddy current loss consumed in the electromagnetic steel sheet based on the homogenization method [28]. For reducing computation time, eddy current loss calculations for all windings, which need a large number of elements, is executed not by 3D-FEA, but 2D-FEA. For the others, eddy current loss computations of an iron core, PMs, frame and bracket are carried out by 3D-FEA.

In order to correctly consider the eddy current losses caused by the current harmonics, the input current waveforms are the current waveforms measured in the experimental tests using an oscilloscope. As an example, U-phase current waveform at the operating point No.4 and FFT spectra of the current waveform are shown in Figs. 16 and 17, respectively. It can be found from Figs. 16 and 17 that the 5th and 7th order current harmonics caused by space harmonics of the machine parameters and high order current harmonics as multiple of 12.5 kHz caused by the PWM carrier frequency are large. The measured FEC current is also used for taking account of current harmonics.
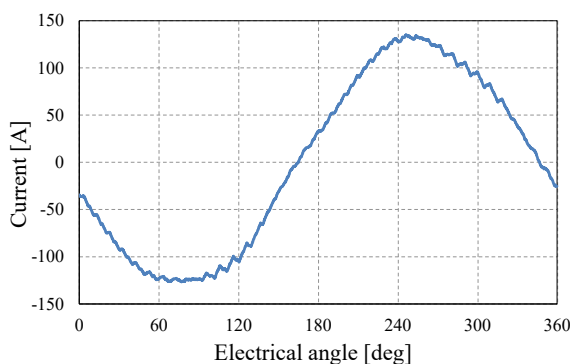

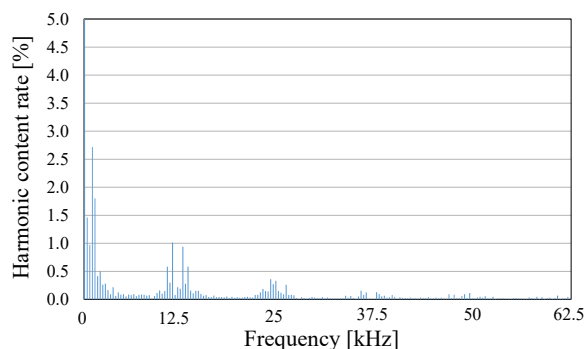Fig. 16. U-phase current waveform at operating point No.4.

Fig.17. FFT spectrum of U-phase current at operating point No.4.

C. Iron Loss Calculation Results

Table VII summarizes the eddy current losses calculated by two different analysis methods. One is based on 2D- and 3D-FEA using the ideal current waveforms as the inputs (hereafter, named as conventional method) and the other is based on 2D- and 3D-FEA using the measured current

waveforms as the inputs (hereafter, named examined method). Table VIII appears the comparison between the calculated and the measured iron losses including hysteresis loss computed by the conventional method [26]. It can be seen from the Tables VII and VIII that the error between the calculated and the measured iron loss can be dramatically reduced by considering the eddy current losses generated in the windings, the PMs, the frame and the bracket. As a result, it is confirmed that the effect of the harmonics of flux density distribution caused by the harmonic currents on the eddy current loss analysis is considerably large. In particular, the eddy current loss of the windings in the newly designed HEFSM employing the high filling factor windings becomes a dominant loss.

Fig. 18 illustrates the eddy current loss distribution in the stator body at the operation point No.4. In comparison with the conventional method, it is found that the eddy current loss in the examined method increases at the teeth and the back yoke where the amplitude of flux density distribution is as large as to be saturated. In the examined method, it is reasonable to suppose that the eddy current loss produced by the harmonics of flux density distribution can be considered. Fig. 19 shows the analysis results of the current and the eddy current loss density distributions of the armature windings and the FECs at the operating point No.4 computed by the examined method. In this figure, the contour diagrams demonstrate the average values of the current and the loss density for one electrical cycle. The current density of the winding near the rotor is high so that the eddy current loss density is correspondingly large. This is because fringing flux increases electromotive force induced in the wires near the rotor. Compared with round wires, the flat-shape rectangular wires have a larger cross-sectional area along with flat shape surface, resulting in more susceptible to this effect. When designing the motor with high filling factor winding using flat-shape rectangular conductors, some figuring out is indispensable to avoid an increase in the current density and eddy current loss due to this effect.

TABLE VII
EDDY CURRENT LOSS IN EACH MOTOR COMPONENT

Analysis method	Operating point No.	Core [W]	Coil (Armature & field) [W]	Permanent magnet [W]	Flame & bracket [W]
Conventional method	2	24.5	73.1	1.4	12.0
	4	116.8	483.3	4.9	36.5
Examined method	2	76.6	81.7	2.0	15.2
	4	202.9	553.7	6.9	39.7

TABLE VIII
COMPARISON BETWEEN MEASURED AND COMPUTED IRON LOSSES

Operating point No.	Analysis method	Measured iron loss P_{imeas} [W]	Analysis result		Difference $(P_{ieddy} + P_{ihys}) - P_{imeas}$	
			Eddy current loss P_{ieddy}[W]	Hysteresis loss P_{ihys} [W]	[W]	[%]
2	Conv. method	309	111	42.8	-155.2	-50
	Examined method		175.5		-90.7	-29
4	Conv. method	1137	641.5	111.7	-383.8	-34
	Examined method		803.2		-222.1	-20

OKADA et al. : HYBRID EXCITATION FLUX SWITCHING MOTOR WITH PERMANENT MAGNET PLACED AT
MIDDLE OF FIELD COIL SLOTS AND HIGH FILLING FACTOR WINDINGS

257

(a) conventional method   (b) examined method

Eddy current loss density [kW/m³]
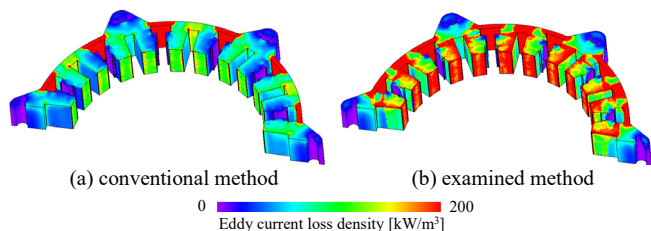
Fig. 18. Eddy current loss distribution in stator at operating point No.4.

(a) current density distribution

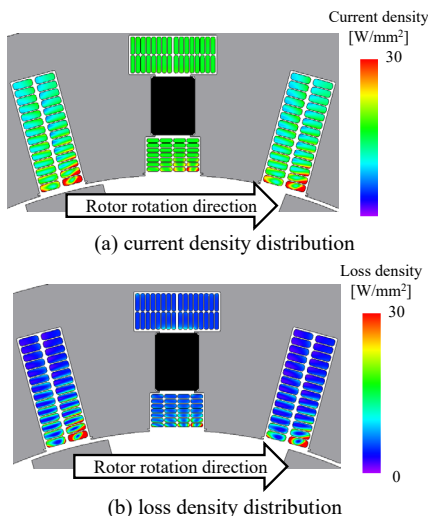

(b) loss density distribution

Fig. 19. Current and loss density distribution in windings at operating point No.4.

VII. CONCLUSION

This paper presented design and experimental studies on HEFSM with PMs placed at middle of FECs slots on the stator. Based on the problems and design trade-off found in the previously designed and tested HEFSM, the design of newly developed HEFSM was figured out by employing new materials such as high filling factor winding, thinner SiFe electromagnetic steel and PMs with high remanent and less amount of Dy used to improve the motor efficiency as a traction motor for a target HEV drive application. The experimental tests using the prototype of 60kW HEFSM built demonstrated that the newly designed HEFSM satisfied the target maximum power and torque as well as achieved motor efficiency better than the IPMSM installed on the third generation Prius IPMSM under the light-load operating condition corresponding to urban cruising of the vehicle. In addition, in order to improve the accuracy of iron loss computation at the design stage, how to reduce the error between the calculated and the measured iron losses was considered. The examined analysis approach will contribute to designing and fabricating HEFSM with even better motor efficiency as a variable flux motor.

REFERENCES

[1]   M. Kamiya: "Development of Traction Drive Motors for the Toyota Hybrid System", *IEEJ Trans. Ind. Appli.*, vol.126-D, no.4, pp.473-479, 2006.

[2]   T. A. Burress, S. L. Campbell, C. L. Coomer, C. W. Ayers, A. A. Wereszczak, J. P. Cunningham, L. D. Marlino, L. E. Seiber and H. T. Lin, "Evaluation of the 2010 TOYOTA PRIUS Hybrid Synergy Drive System", ORNL/TM-2010/253, Oak Ridge National Laboratory, Oak Ridge, Tennessee, 2011.

[3]   M. Arata, Y. Kurihara, D. Misu and M. Matsubara, "EV and HEV Motor Development in TOSHIBA", *IEEJ Journal of Ind. Appl..*, vol. 4, no.3, pp.152-157, 2015.

[4]   E. Hoang, M. Lecrivain, and M. Gabsi, "A New Structure of a Switching Flux Synchronous Polyphased Machine with Hybrid Excitation", Proc. of European Conf. on Power Electronics and Applcations (EPE), no.14, 2007.

[5]   I. Ozawa, T. Kosaka and N. Matsui, "Less Rare-Earth Magnet-High Power Density Hybrid Excitation Motor Designed for Hybrid Electric Vehicle Drives", Proc. of European Conf. on Power Electronics and Applications (EPE), no. 722, 2009.

[6]   G. Zhang, W. Hua, M. Cheng, J. Liao, J. Zhang and W. Jiang, "Investigation of On-Loaded Performance of Hybrid Excitation Flux-Switching Brushless Machines for HEV/EV Applications", Proc. of the Sixth Annual IEEE Energy Conversion Congress and Exhibition (ECCE), pp.328-335, 2014.

[7]   H. Nakane, T. Kosaka and N. Matsui, "Design Studies on Hybrid Excitation Flux Switching Motor with High Power and Torque Densities for HEV Applications", the IEEE International Conference on Electrical Machines and Drives Conference (IEMDC), pp.234-239, 2015.

[8]   T. Kogawa, T. Kosaka and N. Matsui,"Drive Characteristics of HEFSM with Permanent Magnet Placed at Bottom of Slot for Vehicle Propulsion", 2015 IEE-Japan Industry Applications Society Conference, No.3-4, pp. III-79-III-82, 2015 (in Japanese).

[9]   W. Hua, G. Zhang and M. Cheng, "Flux-Regulation Theories and Principles of Hybrid-Excited Flux-Switching Machines", *IEEE Trans. Ind. Electronics*, vol. 62, no. 9, pp.5359-5369, 2015.

[10] H. Hua and Z. Q. Zhu, "Novel Hybrid-Excited Switched-Flux Machine Having Separate Field Winding Stator", *IEEE Trans. Mag.*, vol.52, no.7, 2016.

[11] Y. Maeda, T. Kosaka and N. Matsui, "Design Study on Hybrid Excitation Flux Switching Motor with Permanent Magnet Placed at Middle of Field Coil Slot for HEV Drives", Proc. of International Conference on Electrical Machine (ICEM), pp. 2524-2530, 2016.

[12] H. Yang, Z. Q. Zhu, H. Lin, D. Wu, H. Hua, S. Fang and Y. Huang, "Novel High-Performance Switched Flux Hybrid Magnet Memory Machines with Reduced Rare-Earth Magnets", *IEEE Trans. Ind. Appli.*, vol. 52, no. 5, pp.3901-3915, 2016.

[13] J. H. Kim, M. Liu. H. Ding and B. Sarlioglu, "Comparison of dual structure axial flux-switching permanent magnet machines", Proc. of the Ninth Annual IEEE Energy Conversion Congress and Exhibition (ECCE), pp.328-333, 2017.

[14] Y. Yang, X. Yang, P. Chen and X. Wang, "Electromagnetic Performance Analysis of Hybrid Excited Segmental Rotor Flux Switching Machine", *IEEE Trans. Mag.*, vol.54, no.11, Paper-ID:8106055, 2018

[15] E. Yıldırız, M. Güleç, and M. Aydın, "An Innovative Dual-Rotor Axial-Gap Flux-Switching Permanent-Magnet Machine Topology With Hybrid Excitation", *IEEE Trans. Mag.*, vol.54, no.11, Paper-ID:8107705, 2018.

[16] K. Sakai, N. Yuzawa and H. Hashimoto, "Permanent Magnet Motors Capable of Pole Changing and Three-Torque-Production Mode using Magnetization", *IEEJ Journal of Ind. Appli.*, vol. 2, no. 6, pp.269-275, 2013.

[17] N. Limsuwan, T. Kato, K. Akatsu and R. D. Lorenz, "Design and Evaluation of a Variable-Flux Flux-Intensifying Interior Permanent-Magnet Machine", *IEEE Trans. Ind. Appli.*, vol. 50, no. 2, pp.1015-1023, 2014.

[18] M. Ibrahim, L. Masisi and P. Pillay, "Design of Variable-Flux Permanent-Magnet Machines Using Alnico Magnets", *IEEE Trans. Ind. Appli.*, vol. 51, no. 6, pp.4482-4491, 2015.

[19] H. Yang, H. Lin, Z. Q. Zhu, D. Wang, S. Fang and Y. Huang, "A Variable-Flux Hybrid-PM Switched-Flux Memory Machine for EV/HEV Applications", *IEEE Trans. Ind. Appli.*, vol. 52, no.3, pp.2203-2214, 2016.

[20] H. Hua, Z. Q. Zhu, A. Pride, R. Deodhar and . Sasaki, "Comparative Study of Variable Flux Memory Machines with Parallel and Series Hybrid Magnets", Proc. of the Ninth Annual IEEE Energy Conversion Congress and Exhibition (ECCE), pp. 3942-3949, 2017.

[21] E. Sulaiman, T. Kosaka and N. Matsui, "High Power Density Design of 6Slot-8Pole Hybrid Excitation Flux Switching Motors for Hybrid Electric

Vehicles", IEEE Transactions on Magnetics", Vol. 47, No.10, pp.4453-4456 (2011).

[22] E. Sulaiman, T. Kosaka and N. Matsui, "Design Optimization and Performance of a Novel 6-Slot 5-Pole PMFSM with Hybrid Excitation for Hybrid Electric Vehicle", IEEJ Transactions on Industry Applications, Vol.132, No.2, pp.211-218 (2012).

[23] E. Sulaiman, M. Z. Ahmad, Z. A. Haron and T. Kosaka, "Design studies and performance of HEFSM with various slot-pole combinations for HEV applications", Proc. of the IEEE International Conference on Power and Energy (PECon), pp. 424-429 (2012).

[24] Z. A. Husin, E. Sulaiman and T. Kosaka, "Design studies and effect of various rotor pole number of field excitation flux switching motor for hybrid electric vehicle applications", Proc. of the IEEE 8th International Power Engineering and Optimization Conference (PEOCO), pp. 144-149 (2014).

[25] T. Okada, H. Matsumori, T. Kosaka and N. Matsui, "Hybrid Excitation Flux Switching Motor with Permanent Magnet Placed at Middle of Field Coil Slots Employing High Filling Factor Windings", Proc. of the Tenth Annual IEEE Energy Conversion Congress and Exhibition (ECCE), pp. 4286-4274, 2018.

[26] JSOL Corporation, Avairable: https://www.jmag-international.com/

[27] Hitachi Metals, Ltd., "Magnet and Motor-Related products", Avairable: https://www.hitachi-metals.co.jp/products/auto/el/pdf/magnet_wire.pdf

[28] H. Kaimori, A. Kameari, and K. Fujiwara, "FEM Computation of Magnetic Field and Iron Loss in Laminated Iron Core Using Homogenization Method", *IEEE Trans. Mag.*, vol. 43, no. 4, pp.1405-1408, 2007.

Takeshi Okada was born in Gifu, Japan, in 1995. He received the B.S. degree from Nagoya Institute of Technology (NITech), Nagoya, Japan, in 2018, where he is currently working toward the M.S. degree in the Department of Electrical and Mechanical Engineering.

His main research interests are control and design of variable flux motors.

Mr. Okada is a Student Member of the Institute of Electrical Engineers of Japan (IEEJ).

Hiroaki Matsumori was born in 1988. He received his B.S. and M.S. in Electrical Engineering from Tokyo Metropolitan University in 2011, and 2013, respectively.

He joined Nippon Telegraph and Telephone Corporation Research and Development in 2013.

He received his Ph.D. in Department of Electrical Engineering, Tokyo Metropolitan University, Tokyo, Japan in 2018. After that, he has been with the Department of Electrical and Mechanical Engineering, Nagoya Institute of Technology, Nagoya, Japan. Now he is an assistant professor in the same university.

Takashi Kosaka was born in Aichi, Japan, on December 29, 1968. He received the B.S., M.S., and Ph.D. degrees in electrical and computer engineering from the Nagoya Institute of Technology (NITech), Nagoya, Japan, in 1994, 1996, and 1999, respectively.

Since 1999, he has been with the Department of Electrical and Computer Engineering, NITech, where he is currently a Professor. From 2002 to 2004, he was at the University of Leicester, Leicester, U.K., as a Visiting Research Fellow supported by the Japan Society for the Promotion of Science. His current research interests include design and control of application-oriented electrical machines.

Dr. Kosaka is a Member of the Institute of Electrical and Electronics Engineering (IEEE) as well as Senior Member of the Institute of Electrical Engineers of Japan (IEEJ).

Nobuyuki Matsui was born in Wakayama, Japan, on May 7, 1943. He received the B.S. and M.S. degrees from the Nagoya Institute of Technology (NITech), Nagoya, Japan, in 1966 and 1968, respectively, and the Ph.D. degree from the Tokyo Institute of Technology, Tokyo, Japan, in 1976, all in electrical engineering.

Since 1968, he has been a Professor with the Department of Electrical and Computer Engineering, NITech, and has been engaged in research and education on power electronics and motion control. From April 2000 to October 2002, he was the Vice President of NITech. From January 2004 to March 2010, he was the President of NITech, where he is currently an Emeritus Professor.

Prof. Matsui is a Life Fellow of the Institute of Electrical and Electronics Engineering (IEEE) and a Fellow of the Institute of Electrical Engineers of Japan (IEEJ). He is a recipient of the Outstanding Achievement Award from the IEEE Industry Applications Society in 2005.